

Tuning the nanopore structure and separation behavior of hybrid organosilica membranes

H.L. Castricum (**HIMS**)

G.G. Paradis (**ECN**)

M.C. Mittelmeijer-Hazeleger (**HIMS**)

W. Bras (**NWO**)

G. Eeckhaut (**Janssen Pharmaceutica**)

J.F. Vente (**ECN**)

G. Rothenberg (**HIMS**)

J.E. ten Elshof (**MESA+**)

December 2013

ECN-W--13-064





Contents lists available at ScienceDirect

Microporous and Mesoporous Materials

journal homepage: www.elsevier.com/locate/micromeso

Tuning the nanopore structure and separation behavior of hybrid organosilica membranes



Hessel L. Castricum^{a,b,c,*}, Goulven G. Paradis^c, Marjo C. Mittelmeijer-Hazeleger^a, Wim Bras^d, Guy Eeckhaut^e, Jaap F. Vente^c, Gadi Rothenberg^a, Johan E. ten Elshof^b

^aVan 't Hoff Institute for Molecular Sciences, University of Amsterdam, Science Park 904, 1098 XH Amsterdam, The Netherlands

^bMESA+ Institute for Nanotechnology, University of Twente, P.O. Box 217, 7500 AE Enschede, The Netherlands

^cEnergy research Centre of the Netherlands, P.O. Box 1, 1755 ZG Petten, The Netherlands

^dNetherlands Organization for Scientific Research, DUBBLE@ESRF BP 220, 38043 Grenoble, France

^eJanssen Pharmaceutica, Turnhoutseweg 30, 2340 Beerse, Belgium

ARTICLE INFO

Article history:

Received 14 June 2013

Received in revised form 29 October 2013

Accepted 3 November 2013

Available online 13 November 2013

Keywords:

Hybrid materials

Microporous membrane

Gas separation

Pervaporation

In-situ SAXS

ABSTRACT

The exceptional hydrothermal- and solvent stability of organically linked silica makes it a promising candidate material for molecular separation membranes. Tailoring towards specific separation properties however requires precise control over the pore structure. Here we show that this can be achieved by adjusting the acid-to-Si ratio immediately before the onset of physical drying of the 1,2-bis(triethoxysilyl)ethane-based polymeric colloidal sols. This procedure provides uniform coating conditions and results in defect-free films. The structure development is investigated with in-situ Small-Angle X-ray Scattering, both in a solvent and during film drying. Acid-catalyzed colloidal growth in a solvent is governed by diffusion-limited cluster aggregation for all studied acid concentrations. Upon solvent evaporation, micropores (<2 nm) are formed at low acid concentrations ($H^+ : Si \leq 0.1$). This can be explained by compressive capillary forces exerted by the receding pore liquid. At $H^+ : Si = 1$, reaction-limited cluster aggregation is observed during drying, followed by the formation of pores >2 nm. The compressive forces are balanced by a network strengthened by ongoing condensation reactions, and by the positive charge on the hybrid organosilica. This results in a larger pore size under more acidic conditions. The permselectivity of the supported membranes correlates with the pore structure of the unsupported materials. Thus, the adaptability of the pore structure allows a wider applicability of organosilica membranes in energy-efficient industrial molecular separations.

© 2013 Elsevier Inc. All rights reserved.

1. Introduction

Rapidly increasing energy costs and climate concerns related to fossil fuel-based energy consumption call for drastic efficiency measures. Several strategies are being developed to improve the energy-efficiency of transport, heating, and industry, which each account for equal shares of the worldwide energy demand. In the chemical industry, distillation, especially cryogenic and azeotropic, is an energy intensive process and consumes billions of barrels of oil equivalent yearly. Replacing these inefficient processes by molecular separation with membranes can save up to 50% of energy of specific processes [1]. Numerous activities take place in this field focused on pervaporation of liquid mixtures [2,3] and gas separation [4,5]. A practically applicable membrane process must

* Corresponding author at: Van 't Hoff Institute for Molecular Sciences, University of Amsterdam, Science Park 904, 1098 XH Amsterdam, The Netherlands. Tel.: +31 20 5256493; fax: +31 20 5255608.

E-mail addresses: h.l.castricum@uva.nl, h.l.castricum@gmail.com (H.L. Castricum).

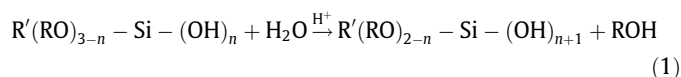
be at least as reliable as the current available technology before it can be implemented on any scale. A major technological challenge is therefore to achieve adequate structural membrane stability. In addition, membranes must be cheap, which implies a small number of simple preparation steps, and preferably be versatile, *i.e.* applicable for different processes and under different conditions.

Recently we have developed a hybrid organosilica-based material that consists of an amorphous network with both organic Si–C_n–Si bridges and inorganic Si–O–Si bonds [6,7]. A one-pot sol–gel procedure allows coating of a <<1 μm-thin selective layer with high permeability on top of a mesoporous support system [8,9]. Pore sizes <1 nm find application for the molecular sieving of small molecules. Long-term chemical and hydrothermal stability has been demonstrated in liquid separation up to 190 °C, in acidic mixtures and in the presence of aggressive organic solvents [10,11]. The solvent- and hydrothermal stability are adequate for nearly all liquid separation processes. Unlike many membranes from organic polymers, permeability, selectivity, and stability are not affected by plasticization effects. With regard to versatility in

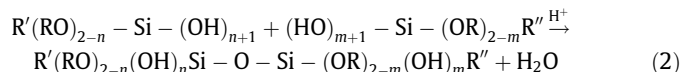
application, the efforts of several research groups are directed at modifying the selectivity, especially in gas separation [12–15]. We recently established how the size, shape, and electronic structure of the organic bridge can be adapted to tailor the separation selectivity for gas and liquid mixtures [16,17]. As a result, separation can now be based both on the relative size of the molecules and on their adsorption properties, *i.e.* the interaction with the pore surface. However, independent and well-controlled variation of the pore size is needed to fully exploit both size-based and affinity-based separation. Small pores are required to separate mixtures of small molecules. Larger pores permit the separation of mixtures of larger molecules, and result in improved permeability. Thus we set out to modify the wet synthesis procedure in order to accurately control the pore size, while retaining a defect-free membrane and avoid the introduction of costly preparation steps.

Here we report a general procedure that allows for adaptation of the pore characteristics, while retaining the optimal rheological coating properties required to obtain defect-free membranes. The key step is adding an acid to a colloidal sol with optimized rheological properties immediately before coating. As the synthesis procedure is straightforward and no surfactants are used, membrane fabrication remains cheap.

Defect-free membranes from alkoxy silanes can only be prepared under acid-catalyzed conditions, *i.e.* below the isoelectric point (IEP). At the IEP, which is at $\text{pH} \sim 2.2$ for SiO_2 [18], the net surface charge (with charged species consisting of $\text{Si}-\text{OH}_2^+$ and $\text{Si}-\text{O}^-$) equals zero. The generalized reactions involved are hydrolysis:



and condensation:



where in $n, m = 0, 1, \text{ or } 2$, R is an alkyl group, and R' and R'' can be various organic groups. The rate of condensation (in which network bonds are formed) is at a minimum around the IEP [19]. Below the IEP, open polymeric structures are formed with a low degree of branching, which, unless a special procedure is followed, give a microporous structure after drying. While the smallest pore size and pore volume result around $\text{pH} \sim 2$, larger values are found at higher acid concentrations [18–20]. The first systematic investigations of pore formation under acidic conditions involved gelled SiO_2 materials with substantial sodium contents [20–24]. The formation of larger pores under more acidic conditions was explained by 'increased aggregation and coalescence of particles as a result of condensation' [23], in which the acid acted as a 'dehydration agent' [22]. More recent studies, related to the preparation of silica membranes from tetraalkoxy silanes, explained the larger pore volumes and -sizes by the packing of the larger and more branched colloids in the sol state [25–30]. At higher acid concentration, larger colloids and higher fractal dimensions D_f were found in SAXS experiments. However, the rheology of such sols was not always found suitable for the preparation of defect-free membranes. Iler also stated that the acid concentration mainly affects the size to which the particles grow before gelation [18]. In short, all these studies relate pore structure to the degree of condensation, expressed in terms of size and branching degree of the colloidal particles, in which more acid gives a higher degree of condensation in the same period. However, the data also suggest a correlation with acid concentration that is independent of the colloid size and structure [27].

By adjusting the acid concentration at the last moment (within a minute before coating), we aimed to establish to what extent the pore structure formation is related to the colloid size, *i.e.* to the

degree of condensation at the onset of drying, and to the acid concentration itself. This procedure assured uniform coating conditions as sols with optimized colloid size distributions were used. Structural effects related to the amount of deposited material were thus avoided. Structure development during the drying process was followed in situ with Small-angle X-ray scattering by means of a specially designed device. To the best of our knowledge, this is the first time that the formation of porous organosilica is studied with any in-situ technique. The structures of unsupported materials were investigated with sorption techniques using various molecular probes. Membrane performances were determined in gas permeation and liquid pervaporation tests. Finally, with long-term applications in mind, hydrothermal, acid, and base stability were assessed using quantitative dissolution tests.

While this study focuses on ethane-bridged materials, which were subjected to extensive membrane tests, the process allows for pore size tailoring of a broad range of silica and hybrid silica membranes. The development of precursors with organic functionalities [31–33] has led to a wide and topical interest in bridged organosilica materials. Controlled variation of the porosity also allows for further fine-tuning of their applicability as low- k dielectrics [34,35], drug-release carriers, sensors, and catalyst supports [36–38].

2. Experimental

2.1. Material preparation

1,2-Bis(triethoxysilyl)ethane (BTESE) was obtained from ABCR. Ultrapure Milli-Q water (18.2 M Ω cm) and HNO_3 (65 wt% in water, Aldrich) were added to dry ethanol, and BTESE was subsequently added to this mixture under vigorous stirring. The mixture was then immediately placed in a water bath at 333 K in a closed glass container. The initial concentration of 1,2-bis(triethoxysilyl)ethane was 0.9 mol/l, the hydrolysis ratio (H_2O :ethoxy) was 1 and the acid-to-silicon ratio ($\text{H}^+:\text{Si}$) was 0.01. The hydrolysis ratio of 1 ensured that hydrolysis was not compositionally limited. After 3 h heating under continuous stirring, the mixture was diluted with an equal amount of ethanol, and split into three portions. The first was used as is, and different amounts of 65 wt% HNO_3 were added to the other two portions. The resulting $\text{H}^+:\text{Si}$ ratios were 0.01 (sol 1), 0.1 (sol 2), and 1 (sol 3). Adding the nitric acid also resulted in a slight increase of the hydrolysis ratio and dilution of the sol. Note that the dilution step with ethanol was not applied in the study of growth and drying processes with in-situ SAXS.

Unsupported xerogel films were obtained by drying the sols in a Petri dish. Supported mesoporous $\gamma\text{-Al}_2\text{O}_3$ membranes were prepared by a dip-coating procedure of a boehmite sol on a 30 cm long tubular $\alpha\text{-Al}_2\text{O}_3$ support system (*i.d./o.d.* = 8/14 mm) [39,40]. The freshly prepared organosilica sols were coated onto this $\gamma\text{-Al}_2\text{O}_3$ layer. Coating procedures were carried out under class 1000 cleanroom conditions to minimize defect formation due to dust particles. All layers were applied on the outside of the tubes. The unsupported and supported films were consolidated by a thermal treatment at 523 K for 2 h in a nitrogen flow (99.999% pure), applying heating and cooling rates of 0.5 K/min. The resulting materials are designated as 'powders' and 'membranes', respectively.

2.2. Characterization of colloidal sols and unsupported films

Colloid sizes in the freshly prepared sols were determined by dynamic light scattering (DLS). The sols were diluted with three volume parts of ethanol and the colloid size distribution was

measured at 298 K using a Malvern Zetasizer Nano ZS. This instrument was also used to determine the zeta potential of sols **1** and **2**.

Small-angle X-ray scattering (SAXS) measurements were carried out at the DUBBLE beamline BM-26B of the European Synchrotron Radiation Facility in Grenoble, France [41]. Scattering data were obtained using 16 keV X-rays. The samples were placed at a distance of 1.5 m from the detector and the intensity was measured with a 2D gas-filled detector. The raw data were corrected for the pixel-dependent detector sensitivity and integrated for channels with the same q values. To investigate the time-dependent structure development of dilute organosilica sols at elevated temperatures, scattering curves of the intensity vs the scattering vector $I(q)-q$ were collected on sols in borosilicate glass sealed capillaries (i.d. = 1.0 mm, glass No. 14, Hilgenberg, Malsfeld, Germany) that were heated to 60 °C in a programmable thermostat (Linkam [42]). Measurements were done with 1–20 min intervals over several hours. An ethanol-filled capillary was used for background correction. In-situ drying experiments were carried out by using a specially designed set-up consisting of a vertically rotating cylinder covered with Kapton foil [43], in which the liquid sol was contained by means of centrifugal force. 5 ml of sol was introduced to produce a liquid layer with a thickness of 1 mm. Scattering patterns were acquired at 1–5 min time intervals. Measurements on powders were obtained by applying them onto a Kapton foil. The scattering pattern of the clean foil under the same conditions was used for background correction. The correlation length L_c [44] was calculated from

$$L_c = \pi \cdot \int_0^\infty I(q) \cdot q \cdot dq / \int_0^\infty I(q) \cdot q^2 dq \quad (3)$$

approximating the low- q regime with an extrapolated Guinier relation $I \sim \exp(-q^2 R_g^2/3)$ and the high- q regime up to $q = 10$ with an extrapolated power-law relation $I \sim q^{-\beta}$. Fourier-Transform Infra Red Spectroscopy on unsupported powders was performed using a Diffuse Reflectance Infrared Fourier Transform cell in a Bio-Rad FT175 at room temperature.

Adsorption/desorption isotherms between 0 and 1 bar were obtained for dried ($p < 10^{-4}$ mbar at 473 K) thermally treated powders on a CE-Instruments Milestone 200. N_2 isotherms were obtained at 77 K, and CO_2 isotherms at 273 K. Surface areas were determined by the Dubinin method, modified by Kaganer [45,46], as in

$$\log n = \log n_m + D (\log p^0/p)^2 \quad (4)$$

with n the gas adsorbed at relative pressure p/p^0 , n_m the monolayer capacity of the surface, both expressed in mol/g adsorbent, and D an adsorbent-dependent constant. The surface areas A were subsequently determined according to

$$A = n_m a_m N_A \quad (5)$$

in which N_A is Avogadro's number and a_m the area occupied by a molecule in the completed monolayer, taken as 0.162 nm² for N_2 (ISO 9277) and 0.179 nm² for CO_2 . The solid skeletal (network) density was determined by gas pycnometry at room temperature, with He as a replacement gas, in a Multivolume Pycnometer 1305 after the same drying procedure.

Acid, hydrothermal, and base stability were determined by exposing 0.3 g of the thermally treated powders for 275 h at 333 K to 10 ml of a 1.0 M HNO_3 solution, Milli-Q water (18.2 M Ω cm), and a 0.1 M NaOH solution, respectively. The fraction of dissolved material was measured with ICP-AES with an error of about 0.1 mg/g.

2.3. Membrane characterization

High resolution Scanning Electron Microscopy was carried out on a Jeol 6330F SEM equipped with a Noran Voyager EDX at a voltage of 5.0 kV.

X-ray Photoelectron Spectroscopy was carried out with a PHI Quantera XPS microprobe from Physical Electronics with an analysis depth of 5–75 Å. The instrument was equipped with a low energy electron flood gun to neutralize the surface. Depth profiles of the concentrations of Si, Al, C, and O inside the membrane were obtained from the Si 2p, Al 2p, C 1s, and O 1s energy bands by sputtering with a 2×2 mm² 3 keV Ar⁺ beam.

Single gas permeation rates of He, H₂, N₂, CO₂, and CH₄ (99.999% pure) were determined at a controlled pressure difference over the membrane $\Delta p = 2$ bar, feed pressures of 3–9 bar(a) and temperatures of 323, 423, and 523 K. Gas modules developed in-house were used in which the temperature inside the tube is measured. The pre-heated gas was fed at the exterior of the membrane tube.

Pervaporation of water from *n*-butanol was carried out using the supported membranes in a stirred vessel at 368 K (95/5 wt% *n*-butanol/water, 1 bar). This composition is of interest to actual dehydration processes as such mixtures are hard to separate otherwise. This gives a large potential reduction in energy cost. Water was continuously added with a pump to correct for the losses. The separation behaviors of the membranes were determined individually at regular intervals with a feed mixture containing 5 wt% demineralized water in *n*-butanol (Merck P.A.). The permeate sides of all membranes were kept at 10 mbar with a vacuum pump. The compositions of the feed and the permeate were determined using the refractive index with the Mettler Toledo Refractometer RA-510 M, calibrated with standard binary mixtures. The separation factor α is defined as:

$$\alpha = (Y_w/Y_b)/(X_w/X_b) \quad (6)$$

with Y and X the weight fractions of water (w) and *n*-butanol (b) in the permeate and feed solutions, respectively.

3. Results

3.1. Sol structure growth and gelation

A polymeric colloidal sol **1** was prepared by acid-catalyzed synthesis of 1,2-bis(triethoxysilyl)ethane. Sol **2** and **3** were prepared by adding a concentrated nitric acid solution to **1**, giving 10 and 100 times higher H⁺:Si ratios, respectively. The clear sols were all at conditions below the IEP of SiO₂, i.e. the surfaces of the colloids were slightly positively charged. This was confirmed by a zeta potential measurement, which gave positive values close to zero (+0.2 mV for sol **1** and +0.5 mV for sol **2**).

The suitability of a sol for thin-film coating is related to the colloid size. With our membrane supports, the mean hydrodynamic diameter d_{hyd} of the colloids must be between 5 nm – larger than the mean pore size of the porous alumina support (3–4 nm) – and 10 nm. Sols with $d_{hyd} > 10$ nm generally result in thick layers that are prone to cracking [7]. Table 1 compares d_{hyd} of sol **1**,

Table 1
Mean hydrodynamic diameters.^a

Sol	d_{hyd} [nm]
1	5.4
2	6.3
3	6.4

^a Sol **1** directly after preparation; **2** and **3** after 1 h at room temperature.

measured before coating, to those of sol **2** and **3** recorded 1 h after adding the acid. The size range is far below the regime at which clusters aggregate to form a continuous network [17]. The broad distributions (see the Supplementary data) indicate polydispersity. Despite the much higher reactivity at higher acid concentration, only a small increase in d_{hyd} is observed after 1 h. This time-scale is much longer than the ~ 1 min that elapsed between acid addition and coating. Therefore, we can conclude that the colloid sizes were sufficiently similar to give sols with effectively equal rheology and coating properties.

The growth process of sols **2** and **3** was followed in situ with Small-Angle X-ray scattering. We used the same conditions as applied in the original synthesis of **1**, *i.e.* before dilution with ethanol. A colloidal sol can be considered to consist of small spherical building blocks that are randomly arranged in a branched polymeric structure. Such assemblies can be described in terms of mass-fractal models [47,48]. The number n of monodisperse spherical building blocks of radius r_0 within an imaginary sphere of effective radius r is $n = (r/r_0)^{D_f}$, in which the packing density is characterized by the so-called fractal dimension D_f . In the initial SAXS patterns a Guinier-like regime is observed at the low- q part, which obeys $I \sim \exp(-q^2 R_g^2/3)$, in which R_g is the gyration radius of an assembly of primary building blocks (Fig. 1). At high q , a power-law relation $I \sim q^{-\beta}$ is observed. For a small colloidal particle, the value of β is related to the degree of branching, and expresses the internal structure of the particle. When this relationship extends over several orders of length scale, it can be interpreted using the fractal dimension D_f . Although in earlier studies on colloidal sols the parameter β has been interpreted as a fractal

dimension [27,49], it should be stressed that ‘fractal’ here is a mathematical term rather than a description of a physical system. In this case, the low- q boundary of the power-law relation indicates the scale up to which the colloidal particles have a branched structure. The q -range of this regime gradually extends towards smaller q with increasing time and is accompanied by an increase of the gyration radius R_g . The process is much faster for sol **3** than for sol **2**. In the final stage, after $t \sim 2$ ks and 15 ks, respectively, the power-law relation extends over the full measured range. At this point, the structures have transformed into continuous network gels. A well-developed sol and a continuous gel have essentially the same structure and thus cannot be distinguished from each other in the measured range, which in real space corresponds to $d = 2\pi/q$ between about 1 to 13 nm. Colloidal growth is also observed from an increase of the correlation length L_C , which is a measure of the average size of the alternating high and low electron-density regions. For sol **2** we calculated an increase in L_C from 0.6 to 1 nm that gradually leveled off, while this process was again an order of magnitude faster for sol **3**.

Fitting the relation $I \sim q^{-\beta}$ to the scattering pattern gives a resulting exponent β of 1.87 ± 0.03 for both sol **2** and **3**, indicating a limited degree of branching. Indeed, the polymeric colloidal particles that result from acid-catalyzed condensation are known to consist of chains with limited branching. Fractal-like structures with a maximum dimension of 1.85 ± 0.1 have been explained by a growth mechanism dominated by Diffusion-Limited Cluster Aggregation (DLCA). In DLCA, the approach of particles is governed by Brownian transport, and reaction is much faster than diffusion. Both monomer–cluster and cluster–cluster aggregation occur [50–52]. This means that clusters of all sizes can bond, which is in line with the broad distributions seen using DLS. Similar maximum values for β were also found in SAXS studies on acid-catalyzed silica [25,50] and Nb/SiO₂ sols [53,54] applied in microporous membranes. DLCA rather than Reaction-Limited Cluster Aggregation (RLCA) also provides the most likely explanation for our data. In RLCA, reaction proceeds more slowly than diffusion, and a maximum β value of around 2.09 is expected [55]. We found similar β values of ~ 1.87 for a wide range of acid concentrations and for various hydrolysis rates (not shown). Such an independence of composition was also observed in a study on SiO₂ elsewhere [25]. We conclude that the DLCA growth process in acid-catalyzed sols from BTESE is similar to that of silica-based sols from tetra-alkoxysilanes, and essentially independent of the acid concentration.

3.2. Organosilica xerogel formation during solvent removal

In the open literature, no single method is described so far for the in-situ observation of the formation of a spatially continuous porous structure from a colloidal state. If one wants to study such nm-scale processes using X-rays one has to revert to high intensity synchrotron radiation beamlines in order to obtain the appropriate time-resolution. A drawback in this case is that the samples have to be mounted vertically. This obviously has some implications when one wants to study a drying process. To overcome this problem we used a specially built cell, in which the liquid sol was contained in a rotating cylinder with a kapton window in which the drying liquid was evenly distributed by means of the centrifugal force. This allowed us to follow the drying process of the liquid organosilica sols **1**, **2**, and **3** (again at the same Si concentration as applied in the original synthesis of sol **1**) to dried xerogels.

As expected from the DLS study, the initial scattering profiles of the three data series, acquired during the first 150 s of drying, are similar (Fig. 2). The Guinier region extends from the lowest q range up to $q \sim 1.1 \text{ nm}^{-1}$, while the power-law range was observed at higher q (indicated in Fig. 2a). This value corresponds to a real-space dimension of $\sim 5.7 \text{ nm}$, which agrees with the hydrodynamic

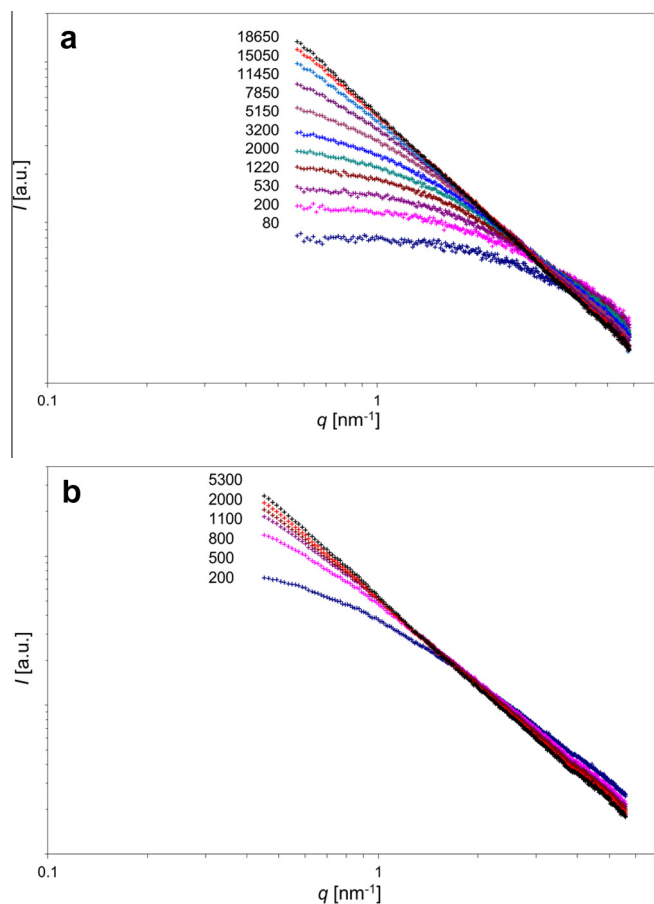


Fig. 1. Small-angle X-ray scattering patterns of colloidal sols (a) **2** and (b) **3** held at 333 K for the indicated times (seconds).

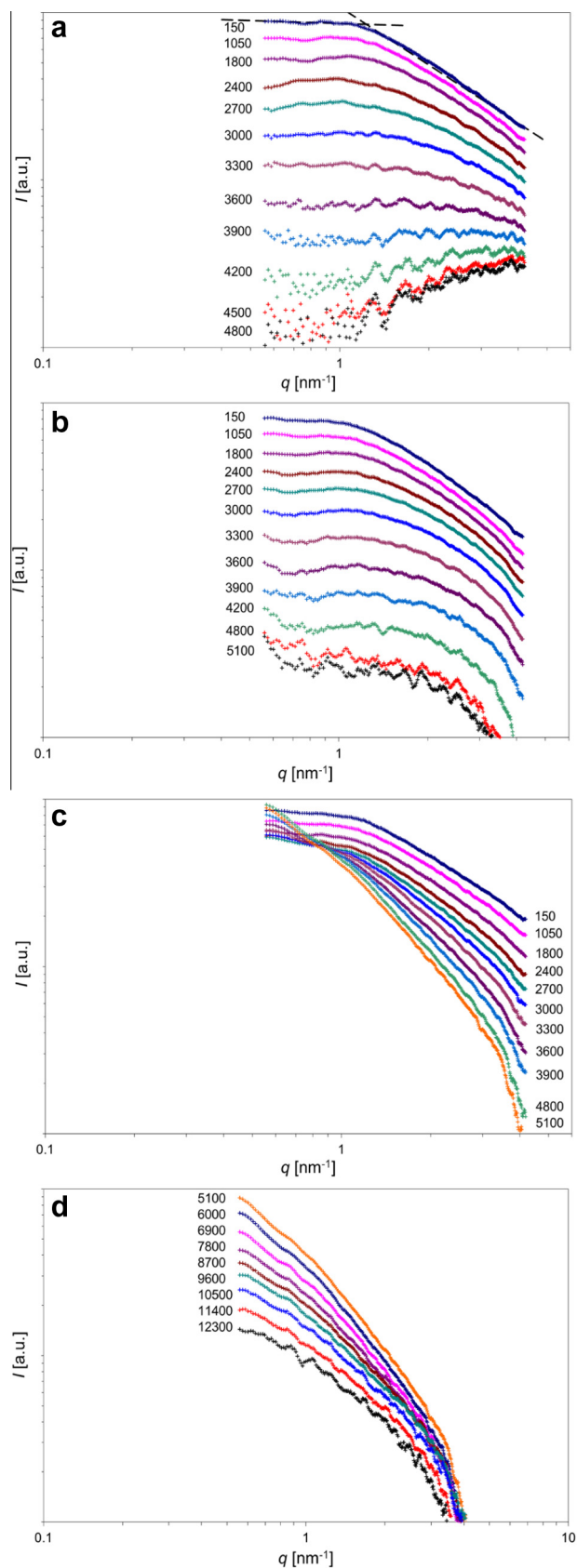


Fig. 2. Small-angle X-ray scattering patterns of colloidal sols acquired during in-situ drying at room temperature: (a) **1**, (b) **2**, (c) and (d) **3**. The indicated times are in seconds.

diameter of the colloids determined with DLS (Table 1). The exponent β of the power-law relation above $q = 1.1 \text{ nm}^{-1}$ has a value of

about 1.2, indicating a low branching degree of the colloids. In the first 2 ks, solvent evaporation only leads to concentration of the colloids. While this gives a lower X-ray scattering contrast and reduces the intensity, the sol structure remains essentially unchanged. Substantial changes are only observed after 2 ks.

For sol **1**, we see a further decrease of the total (background-corrected) scattering intensity and a concomitant increase of the noise (Fig. 2a). The exponent of the power-law relation β drops to (below) zero within 1 h. The nearly complete disappearance of the electron density contrast can be interpreted as the formation of a material that is fully homogeneous on this length scale. The negative value of β is related to scattering as a result of local and thermal density fluctuations [56]. As these short-range fluctuations are most prominent at the atomic scale, the scattering intensity increases towards higher q . For the other drying sols, other structural arrangements result in relatively strong scattering that obscures these short-range density fluctuations. The profile remains unchanged after 4.5 ks.

For sol **2**, we see similar events, except that the exponent remains slightly positive, while it is substantially larger at the high- q part of the pattern (Fig. 2b). The exact value at high q could however not be determined due to the low signal-to-noise ratio in this range.

The initial development of sol **3** looks similar to that of sols **1** and **2**, but from ~ 2 ks after the onset of drying, a shift of the point of inflection between the Guinier and power-law regimes is observed towards lower q (Fig. 2c). This is accompanied by an increase of β . These observations indicate a continuation of the growth process at room temperature as the result of ongoing condensation reactions. The process is likely accelerated by the presence of a substantial amount of acid catalyst and by solvent evaporation, which further concentrates the reactants. A maximum value for β of 2.15 ± 0.1 is found, which is significantly higher than the 1.87 observed when no solvent evaporation occurs. After $t \sim 5$ ks, the scattering intensity decreases and β eventually drops to 1.5 (Fig. 2d). As $\beta > 3$ at the high- q part of the pattern, this indicates a surface fractal on the $< 2 \text{ nm}$ scale.

The development of β as a function of time is summarized in Fig. 3, with negative values displayed as zero. A homogeneous material on the nm scale is formed from sol **1**. Sol **2** results in a mass fractal structure with a low dimensionality. For sol **3**, the high value of β after $t \sim 4$ ks indicates that colloidal growth attains the character of reaction-limited aggregation [55]. This change from DLCA to an RLCA-type process upon solvent evaporation can be understood by realizing that the mutual approach of the colloids due to evaporation attains a non-Brownian character. The decrease of the scattering intensity after $t \sim 5$ ks indicates densification of

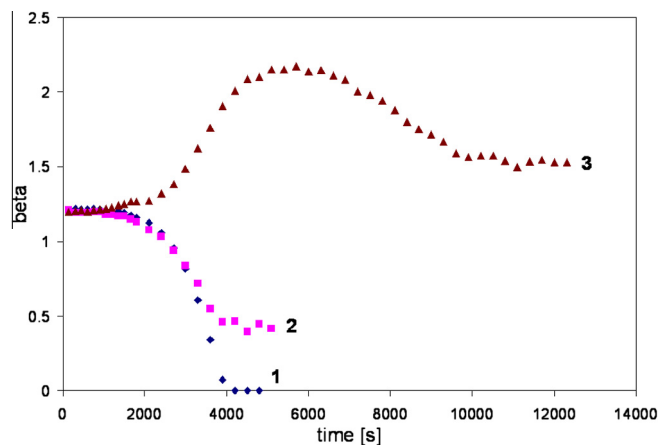


Fig. 3. Coefficient β of the relation $I \sim q^{-\beta}$ fitted to the SAXS patterns in Fig. 2.

the structure, although to a lesser extent than for **1** and **2**. While the resulting structure shows similarities with a mass fractal, the more homogeneous character at larger length scales and the surface fractal at smaller ones can be interpreted in terms of a pore structure with an upper limit in the size distribution. The correlation lengths L_C increased from 0.7 to 1.5 nm for sol **2** and to 2 nm for sol **3** during the drying process (see the [Supplementary data](#)). This redistribution of electron density contrast can similarly be interpreted as the formation of a porous structure.

The structures remain essentially intact after thermal treatment ([Fig. 4](#)). The SAXS pattern of powder **1** shows again a ‘negative’ value for β . The slope at $q < 0.5 \text{ nm}^{-1}$ suggests scattering related to the surface of the μm -sized powder particles that becomes visible due to the low overall intensity of the scattering profile. For the thermally treated powder **2**, the power-law relation extends down to $q = 1.5 \text{ nm}^{-1}$, with $\beta = 1.6$, somewhat larger than for the fresh xerogel. Powder **3** exhibits a mass fractal below $q = 2.4 \text{ nm}^{-1}$ and a rough surface fractal ($3 < \beta < 4$) above. The increase in β after thermal treatment for **2** and **3** can be related to the further removal of solvent and water molecules, which increases the electron contrast. This was confirmed for a xerogel **3** that had been formed after 3 h drying at room temperature. After subsequent heating to 333 K during 1 h, the scattering pattern was similar to that of the thermally treated powder **3** in [Fig. 4](#), while the pattern returned to the one observed before heating after ‘rewetting’ the material with H_2O or ethanol. This process was found to be reversible upon reheating.

We also investigated in situ the drying process of wet gels that were produced by aging sol **1** and sol **3**. These materials had undergone condensation to a substantial extent, resulting in the formation of continuous networks. They thus did not consist of individual nm-sized particles. For wet gel **1** we observed a gradual decrease of the scattering intensity and a drop of β to below zero. This again indicates the formation of a material that is fully homogeneous on this length scale. Likewise, similar mass-fractal structures were produced from a sol and a wet gel from **3**. The final structure thus does not depend on the colloid size or on the state at the onset of drying. This is further discussed in Section 4. No difference in final structure was found for whether the acid was added in the initial stage of synthesis or at the onset of drying. A xerogel structure similar to that from sol **3** was also formed at a hydrolysis ratio of exactly unity (instead of slightly larger due to the addition of water from the nitric acid solution) and $\text{H}^+:\text{Si} = 1$. This indicates a dominant role of the acid concentration in structure formation.

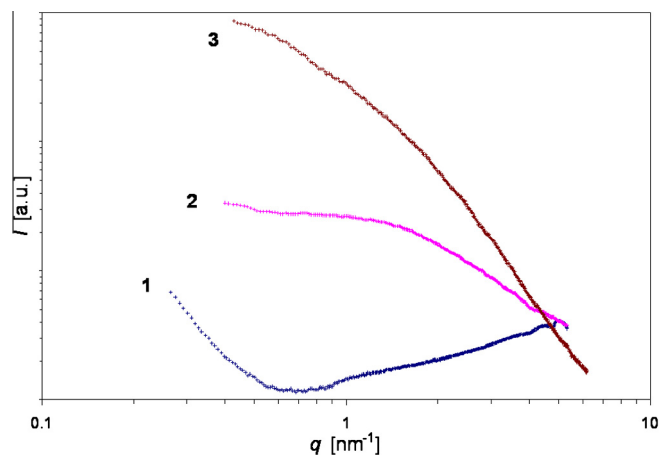


Fig. 4. Small-angle X-ray scattering patterns of the thermally treated powders **1**, **2**, and **3**.

3.3. Organosilica nanostructure

The symmetric and asymmetric stretching bands of the C–H bonds of CH_2 in the thermally treated powders were observed between 2800 and 3000 cm^{-1} with FTIR spectroscopy ([Fig. 5](#)). No indications of organic decomposition were found. The 3000–3700 cm^{-1} band corresponds to the –OH stretching modes of water and shows intensities of the same order for the three materials. Considering that the storage conditions (ambient air) prior to measurement were identical, the amount of adsorbed water, and thus the hydrophilicity of the materials, was comparable. A peak at 3726 cm^{-1} is observed for powder **3**, and appears as a shoulder for **2**. This peak was associated with hydroxyl groups bound to Si with a weakly acidic character [57], as well as with hydroxonium or $\text{H}^+(\text{H}_2\text{O})_x$ [58]. This suggests that H^+ from the nitric acid is still present in the organosilica network after thermal treatment at 523 K.

The skeletal density was probed with He pycnometry. A value of 1.7 g/cm^3 was found for powders **2** and **3**, which scales with an earlier reported value for this type of material [17]. The value is lower than that of pure silica, *i.e.* 2.2 g/cm^3 , which is related to the presence of the organic bridging groups. A slightly lower value of 1.6 g/cm^3 was found for powder **1**. The equilibration process took substantially longer for this material, indicating very small pores.

The pore structure was investigated with vapor adsorption, using both N_2 and CO_2 as molecular probes. With N_2 , zero (*i.e.* below the detection limit) surface area and pore volume were found for powder **1**. For **2** and **3**, the N_2 isotherms were of type I, indicating microporosity. Additional hysteresis was observed for **3** ([Fig. 6](#)), which indicates larger pores than for **2**. With CO_2 , non-zero surface areas were observed for all materials, including **1**. Considering that the kinetic diameters of N_2 and CO_2 are of the same order, the high sensitivity to the size of the pore entrance is likely related to the low temperature of N_2 adsorption. While CO_2 adsorbed at 273 K, N_2 adsorption was measured at 77 K, at which temperature more kinetic hindrance of molecular transport into the pores occurs. Unlike N_2 , CO_2 does not exhibit pore filling under the applied conditions. The high surface areas found with N_2 adsorption for **2** and **3** are therefore likely an overestimation related to the filling of supermicropores. The CO_2 surface areas of the three materials are comparable and are in fact nearly equal for **2** and **3** ([Table 2](#)). This suggests that the surface structure of the materials is similar, even though they differ in pore size. The lower density and long equilibration time observed with He pycnometry

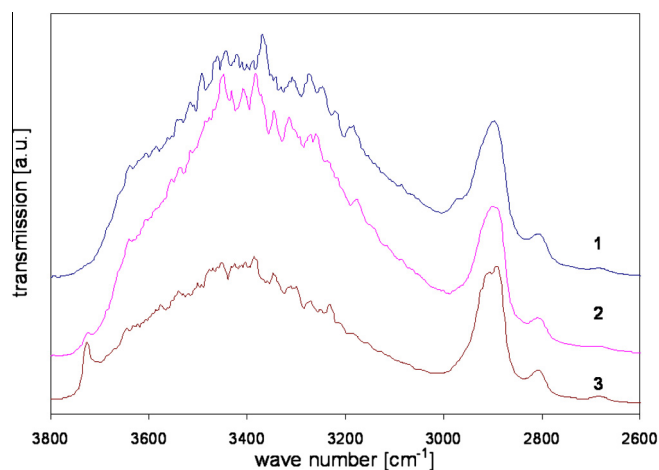


Fig. 5. High-frequency Fourier Transform IR spectra of thermally treated powders, displaying the symmetric and asymmetric stretching bands of the C–H bonds of the ethane bridges and the water absorption band.

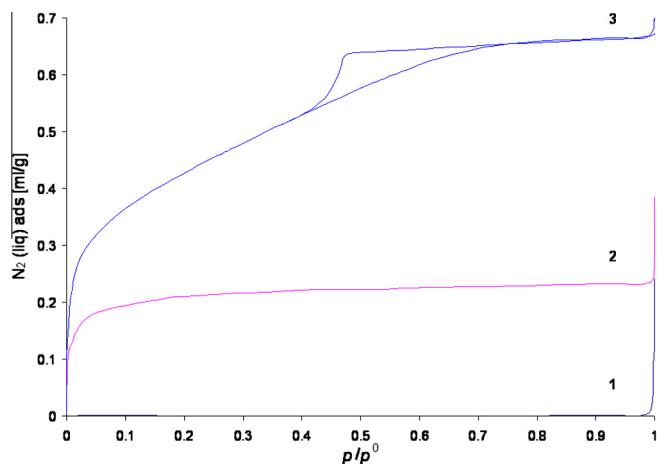


Fig. 6. N_2 adsorption isotherms of the thermally treated powders **1**, **2**, and **3**.

Table 2

Pore volume and surface area determined by N_2 adsorption at 77 K, and mean pore diameter d_p calculated from these values; surface area determined by CO_2 adsorption at 273 K.

Powder	v_p [ml/g]	A_{N_2} [m ² /g]	d_p [nm]	A_{CO_2} [m ² /g]
1	0	0 ^a	–	318
2	0.234	632	1.48	376
3	0.665	970	2.74	375

^a Below the detection limit, i.e. <10 m²/g.

may explain the lower A_{CO_2} of powder **1** as due to closed porosity, i.e. pore entrances smaller than the kinetic diameter of the probe molecules. Mean pore diameters $d_p = 4v_p/A$ were estimated from the surface area A_{N_2} and the pore volume v_p and are given in Table 2. Powder **2** had a typical microporous character, but **3** cannot be considered as strictly microporous, as $d_p > 2$ nm.

The high resistance to acids and the hydrothermal stability of bridged organosilica membranes makes them very suitable for application in liquid separation processes [11]. To assess to what extent variation of the pore size could affect their applicability, we determined the solvolytic stability of the powders under hydrothermal, acidic, and basic conditions. The fractions of material dissolved after 275 h at 333 K are displayed in Table 3, along with those of SiO_2 prepared from tetraethylorthosilicate with a $H^+ : Si$ ratio of 0.1. The composition of the latter material is comparable to that applied in SiO_2 membranes [59,60]. Note that all three organosilicas were stable under neutral and acid conditions, and less stable under basic ones. The amounts of dissolved material were up to an order of magnitude higher for SiO_2 . The somewhat lower values found for **1** may be related to its dense pore structure, which delays transport from and into the solution. The even better solvolytic stability at pH = 0 than at pH = 7 confirms that the materials are suitable for application under acid conditions. We conclude that the applicability under hydrothermal and acid conditions is not affected by variation of the pore size.

Table 3

Fraction [%; mg/g] of material that was dissolved into 10 ml of the indicated solutions after 275 h at 333 K for thermally treated organosilica and SiO_2 .

Powder	1 M HNO_3	H_2O	0.1 M NaOH
1	0.05	0.08	9.7
2	0.10	0.23	14.0
3	0.11	0.36	17.6
SiO_2	1.14	1.44	64.3

3.4. Membrane structure, gas permeation, and pervaporation performance

Supported membranes were prepared that were optically defect-free after thermal treatment. Thicknesses of the selective layers as determined with SEM are summarized in Table 4. The top part of membrane **3** is shown in Fig. 7. The difference in elemental composition of the top layer (Si) and that of the lower layers (Al) was confirmed with Energy Dispersive X-ray spectroscopy. The thicknesses of membrane **1** and **2** were, within the error margin, equal, while that of membrane **3** was substantially larger. This cannot be explained by the small differences in concentration, density, and viscosity related to the composition of the coating sols, as these can be calculated to rather lead to a ~6% thinner layer for **3**.

Depth profiles of the elemental composition of membranes **1** and **3** were recorded with XPS (Fig. 8). After 17.5 and 18.5 min of sputtering with Ar^+ , respectively, the interface between Si and Al was reached. As the sputtering times before reaching this support were similar, the organosilica layers contained similar numbers of atoms. The substantial difference in layer thickness determined with SEM can be accounted for when we assume a comparable difference in pore volume as that determined for the unsupported materials. The chemical composition of the two organosilica layers was similar. The C 1s, O 1s, and Si 2p binding energies were comparable to those of polydimethylsiloxane [61], of which the chemical structure corresponds well to that of our materials. At the interface, the O 1s binding energy shifts to the value corresponding to Al_2O_3 . The top layer of membrane **3** is enriched in Al. This could be related to the high acid concentration in sol **3**, which allows some dissolution of $\gamma-Al_2O_3$ from the interlayer into the organosilica sol upon coating. The Al enrichment could be advantageous for the hydrothermal stability [62–64] and specific permselectivity [65] of the membranes.

The gas permeances of H_2 , He, CO_2 , N_2 , and CH_4 were measured at different pressures and temperatures. For membrane **1** and **2**, the permeances were independent of the average pressure. For membrane **3**, however, the permeances increased at higher pressures. This indicates a less size-sieving character than for membranes **1** and **2**. The relative permeance increase was largest at 523 K and for the largest molecules (N_2 and CH_4). As the permeance was independent of the pressure for small molecules (H_2 , He) at 323 K, the observation cannot be explained by defect-related viscous flow. Indeed, He leak tests showed that none of the membranes had a significant number of macroscopic defects. Moreover, control measurements before and after the whole procedure were identical, showing that no irreversible structure changes occurred in any of the membranes during the measurements. The pressure-dependent permeance increase suggests a reversible change of the pore structure and may be associated with a greater flexibility of the organic bridges in the material at higher temperatures. While all gas permeances increased at higher temperature, those of CO_2 decreased. The behavior of CO_2 can be explained by a more negative enthalpy of adsorption onto the surface, and is related to the presence of surface Si–OH groups [17]. Similar positive apparent activation energies E_{app} were observed for H_2 and He in the three membranes (Fig. 9). For the larger molecules CO_2 , N_2 , and CH_4 , E_{app} increased for the sequence **1**, **2**, and **3**.

The H_2 permeances at 523 K were between $5 \cdot 10^{-7}$ and $9 \cdot 10^{-7}$ mol $m^{-2} Pa^{-1} s^{-1}$, which is of the same order as for other sol-gel-derived SiO_2 [59,66] and hybrid organosilica membranes [12,13,17]. The substantially higher H_2 permeability P_{H_2} of **3** (the product of the permeance and the thickness of the organosilica layer, Table 4) can be explained by a larger pore size, similar as for the unsupported material (Table 2). The permeabilities of all gases are reported in table S1 (Supplementary data).

Table 4

Thickness t_m of the organosilica membrane top layer, H_2 gas permeability P_{H_2} at 523 K and H_2/N_2 , CO_2/H_2 and CO_2/CH_4 permeance ratios at 3 bar feed pressure and a pressure difference of 2 bar.

Membrane	t_m [nm]	P_{H_2} [10^{-15} mol m $^{-2}$ m Pa $^{-1}$ s $^{-1}$]	H_2/N_2 (523 K)	H_2/N_2 (323 K)	CO_2/H_2 (323 K)	CO_2/CH_4 (323 K)
1	219	115	24	19	0.75	13
2	199	126	27	22	0.64	16
3	326	298	11	16	0.64	10

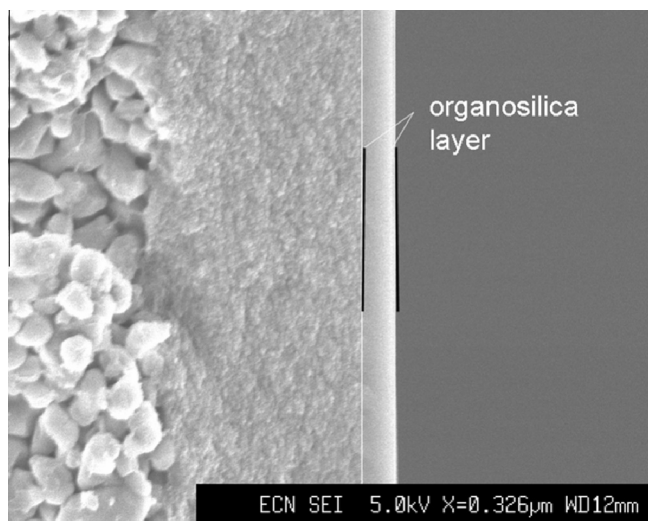


Fig. 7. Cross-sectional scanning electron micrograph of membrane **3**, showing from left to right the macroporous α - Al_2O_3 support layer, the mesoporous γ - Al_2O_3 interlayer and the organosilica top layer. The top layer has a thickness t_m of 326 nm.

The H_2/N_2 , CO_2/H_2 , and CO_2/CH_4 permeance ratios (Table 4) were similar for membranes **1** and **2**, but the H_2/N_2 ratio at 523 K was substantially lower for membrane **3**. As this ratio is only governed by size effects, this confirms the larger pore size of membrane **3**. The H_2/N_2 ratio at 323 K is higher for membrane **3**, and somewhat lower for membranes **1** and **2**. While the behavior for membranes **1** and **2** is typical for molecular sieving membranes, the temperature dependency of this ratio for membrane **3** could again be explained by greater network flexibility at 523 K. This allows the larger N_2 molecule to pass more easily, and agrees with the pressure-dependent permeation behavior under these conditions. For all membranes, the CO_2/H_2 permeance ratios (323 K) are larger than that predicted for Knudsen diffusion (0.21), which is based on the difference in molecular weight. For sieving based on the relative sizes of the molecules, this ratio would even be smaller. This is another indication of a specific interaction of CO_2 with the surface of the materials. The CO_2/CH_4 permeance ratio is also governed by this interaction, as well as by the size difference. For all three membranes, both the CO_2/H_2 and the CO_2/CH_4 permeance ratios decrease at higher temperature, as the specific surface interaction with CO_2 becomes weaker.

Results obtained for a pervaporation process, in which water was separated from a 95/5 wt% mixture of *n*-butanol/water at 368 K, are shown in Table 5. The highest separation factor for this process was observed for membrane **1**, and the lowest one for membrane **3**. The total flux is highest for membrane **3**, despite its greater thickness. This is in line with its higher H_2 permeability, and with the larger pore size of the unsupported material. While the gas permeance ratios of membrane **1** and **2** were similar, the separation factor α in pervaporation differed substantially. Even for membrane **3**, α was still reasonable for this process. Apparently, its pore size was still sufficiently small, and/or the surface sufficiently hydrophilic to block transport of most of the *n*-butanol.

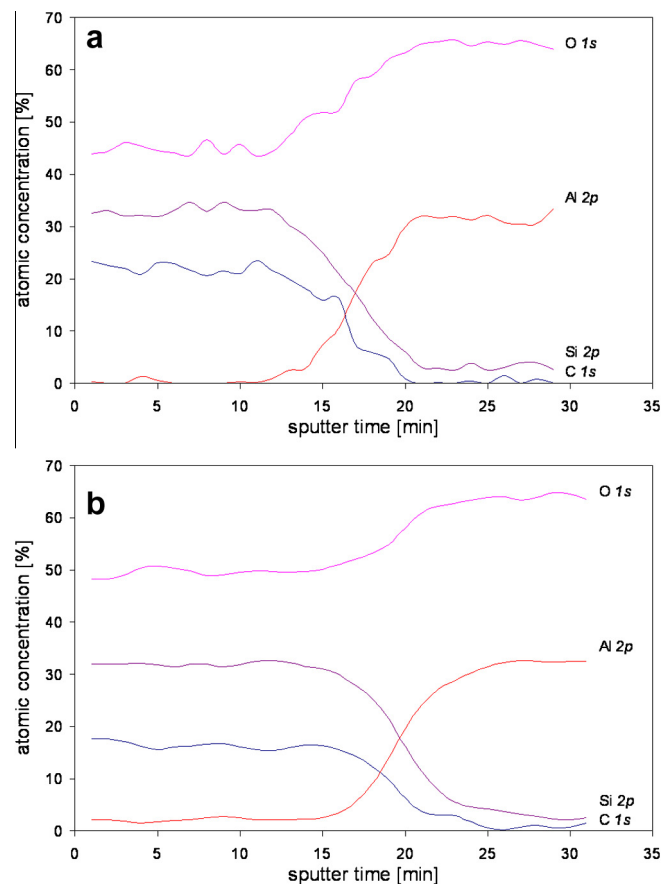


Fig. 8. Depth profiles of the concentrations of Si, Al, O, and C of membranes (a) **1** and (b) **3** as a function of sputter time, determined by X-ray photoelectron spectroscopy.

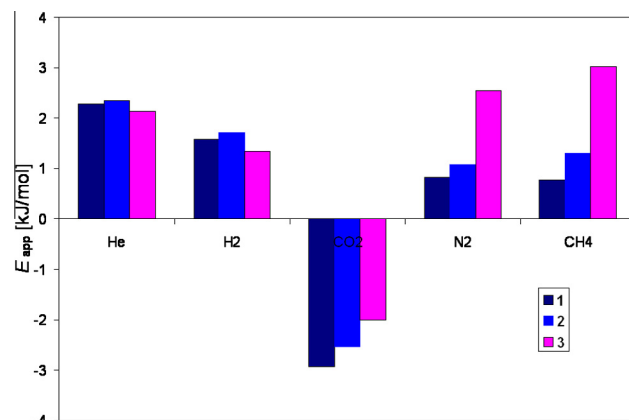


Fig. 9. Apparent activation energies E_{app} of gas permeances through organosilica membranes **1**, **2**, and **3** determined at 3 bar feed pressure and a pressure difference $\Delta p = 2$ bar over the membrane.

Table 5

Water and *n*-butanol fluxes, water content of the permeate, and H₂O separation factor α upon pervaporation of 95/5 wt% *n*-butanol/water (368 K).

Membrane	Water flux [kg m ⁻² h ⁻¹]	<i>n</i> -Butanol flux [kg m ⁻² h ⁻¹]	H ₂ O in permeate[%]	α
1	2.8	0.01	99.7	7.9·10 ³
2	3.4	0.08	97.7	837
3	3.7	0.23	94.2	306

The somewhat larger pore size potentially makes this membrane suitable for the separation of larger molecules.

4. Discussion

Our results show the formation of larger pore volumes and wider pores when there is a higher acid concentration during the drying process. Very small pores and pore entrances, and even closed pores, were observed for unsupported material **1**. For **2**, we found a microporous structure and for **3** pores >2 nm. In conjunction with the pore size increase, the molecular sieving properties of the corresponding supported membranes decline from **1** to **3**. The trend is obvious for the H₂O/*n*-butanol liquid pervaporation process, which displays water separation factors in the order $\alpha_1 > \alpha_2 > \alpha_3$. Considering that liquid separation usually proceeds through surface diffusion processes, the hydrophilic nature of the Si–OH groups at the organosilica surface likely also contributes to high separation factors. However, FTIR measurements showed no indications of relevant differences in hydrophilicity. As the *n*-butanol molecule is substantially larger than water, we conclude that the differences in pervaporation selectivity are governed by the pore size distributions of the membranes.

The H₂/N₂ gas permeance ratios of **1** and **2** are nearly equal, displaying values of about 25 for both membranes. For a separation process in the Henry regime (*i.e.* for dilute non-condensable gases), no competitive adsorption takes place, and the permeance ratio is highly sensitive to the pore size distribution. High values are only obtained if the majority of the pores is smaller than the kinetic diameter of the largest molecule. Much higher H₂/N₂ permeance ratios are generally found for SiO₂ membranes [66]. Computer simulations have confirmed that the presence of ethane bridges in the organosilica material gives rise to wider structural units than in SiO₂ [67,68]. The similarity of the permeation properties of membranes **1** and **2** to small gas molecules may be interpreted as due to an inherent structural limitation to the pore size. While the structural units in BTESE-based membranes allow some transport of N₂, that of larger molecules, including *n*-butanol and SF₆ [13], is still effectively blocked. The substantially lower H₂/N₂ ratios observed for membrane **3** than for **1** and **2** are again in line with its larger pore size. The pressure- and temperature-dependent permeation behavior of N₂ and CH₄ suggests a greater flexibility of the organic bridges at higher temperature that is likely related to the larger pore volume of this membrane. The permeance of CO₂ is governed by surface diffusion processes and is related to strong interaction with the Si–OH groups at the membrane surface [17]. This explains why the CO₂/H₂ permeance ratios were in the same range for all three membranes. By changing the pore size, we can thus specifically adjust the size-based permeation properties, leaving those based on differences in affinity unchanged. In the latter type of separation, larger pores would be preferred as they result in higher permeances.

To assess what processes are responsible for the differences in structure, we first consider colloid growth in the presence of the solvent. We observed that acid-catalyzed condensation in dilute systems eventually leads to similar network structures, irrespective of the concentration of the reactants or of the catalyst. Only

the growth rate differs under these conditions. The formation process is characteristic of Diffusion-Limited Cluster Aggregation. We thus confirmed that the colloid size and internal structure observed with SAXS in earlier studies [25–30,49] are essentially a measure of the degree of condensation of the silica precursor.

Structural differences appear upon drying, after an induction period in which only solvent evaporation occurs. As a result, the concentration of the reactant and the reactivity towards condensation increase. The ongoing condensation reactions in sol **3** showed characteristics of Reaction-Limited Cluster Aggregation. While some densification of the structure of **3** was observed upon further solvent evaporation, the materials from sol **1** and **2** densified to a greater extent. It can be suggested that the formation of larger pores is associated with the RLCA process. For colloidal sols **1** and **2**, enhanced transport would also lead to a reaction limited regime. However, the reactivity of these sols remains too low to result in a structure that shows these characteristics, and only densification was observed.

An alternative explanation for the differences in structure is a different packing of the colloids. Interpenetration of the colloids can occur upon solvent evaporation for low values of β , as explained by De Lange [25] and Brinker [69]. The larger value of β attained for sol **3** would thus imply some ‘hard-sphere’ packing during drying, resulting in the formation of larger pores. However, drying of the continuous gelled networks shows the same structural differences. Similarly as the slightly branched sol, a wet gel from **1** densified to a xerogel that is fully homogeneous on the 1–10 nm scale, while both a sol and a gel from **3** formed xerogels with similar mass-fractal structures. Thus, neither the RLCA process nor colloid size and packing models can explain the differences in xerogel structure.

The similarity in the surface areas observed with CO₂ adsorption suggests that the basic structural units are essentially the same and that only the pore dimensions differ. The difference between the three materials is therefore likely related to densification processes during drying. Densification during xerogel formation is the result of capillary pressure [18,19], which leads to pore contraction. Only at very low or zero capillary pressure, *e.g.* in a supercritical liquid, an open (aerogel) structure with large pores can be formed. Our results hint at a process that induces resistance to the Van der Waals and capillary forces upon drying at increased acid concentration. We postulate two distinct mechanisms that contribute to the formation of larger pores. These mechanisms are related to network strength and charge on the network.

The first mechanism is based on an increase of the network strength at a higher degree of condensation [19]. We observed ongoing condensation upon drying for sol **3**, at high acid concentration. This can lead to gelation of a sol when a large part of the solvent has evaporated but before capillary pressures have increased enough to cause network collapse. As the condensation processes continue after gelation, this leads to further strengthening of the network structure. The development of a surface fractal on the <2 nm scale suggests a ripening process of smaller structural units, which may similarly be explained by ongoing condensation reactions. The network strength is also enhanced by longer drying times, as observed in a Petri dish and during in-situ SAXS, which can be related to the lower vapor pressure of the HNO₃-containing pore liquid. At lower acid concentration, the solvent has evaporated before a similar network strength has developed. In short, increasing the acid concentration makes the material stronger due to the ongoing condensation reactions before the solvent has receded from the pores. However, as no difference was found between a sol and a wet gel from **1**, the strength of a freshly formed continuous network for this composition is insufficient to resist collapse. Thus, to explain our observations, it is plausible that an additional factor is involved.

The second mechanism is related to the positive charge on the network surface below the isoelectric point. The DLVO (Derjaguin, Landau, Verwey, and Overbeek) theory for colloidal systems predicts structure collapse at the IEP [70,71]. Silica colloidal sols, however, are highly stable around the IEP [19]. This well-known anomaly of silica is related to the small values of the static and dynamic parts of the Hamaker constant [72]. As a consequence, screening by a layer of solvent molecules impedes coagulation of the colloids. Upon evaporation of the solvent, this layer disappears. At the IEP, attractive Van der Waals forces and high capillary pressures remain that are only opposed by the strength and elasticity of the formed network. Below the IEP, the surface groups of the (colloidal) network become more positively charged. Electrostatic repulsion reduces the net compressive forces, which leads to larger pores. Indeed, we observed extensive collapse of the material of composition **1**, which is closest to the IEP, and larger pores for compositions **2** and **3** that are more positively charged. FTIR indicated that the acidity remained present after drying and thermal treatment.

Thin-film drying occurs in seconds. It is orders of magnitude faster than the drying of unsupported materials. Faster drying provides less time for network growth before capillary forces become prominent. This would lead to a weaker network, more extensive collapse and smaller pores. The differences in membrane selectivity however indicate that the structural differences were also substantial for thin layers, and can be regarded as another indication of the role of the charge in structure formation.

Summarizing, in-situ observations show that the acid concentration during drying, rather than the size and internal structure of the colloids, determines the size of the pores. In a dilute system, the acid concentration only governs the reaction rate of network formation, while the resulting structures are similar. Structural differences take effect when the solvent is removed. With no net charge present on the colloids, the surface can collapse upon disappearance of the solvation layer. A higher acid concentration results in increased network strength and in a positive charge on the colloids, which reduce the net compressive forces upon solvent evaporation. Despite differences in the basic structural unit, we believe that our results are applicable to all acid-prepared silica and hybrid silica-based materials.

While new liquid separations can likely be readily developed as the result of this work, not all reported single gas permeance ratios will yet allow economical applicability. Still, further optimization of the reported procedures may also result in suitable gas separation applications.

5. Conclusions

The pore size of organically bridged materials was varied by the addition of acid prior to physical drying. This procedure resulted in similar thin-film coating conditions. A larger acid content correlated with a larger pore size for both unsupported materials and supported membranes. This gives lower size-based gas permeance ratios and a higher permeability, leaving the permeance ratios governed by affinity-related surface diffusion unchanged. Size-governed H₂/N₂ gas permeance ratios were limited by the structure of the material on an atomic scale rather than by nm-sized pores. The atom-scale structure is somewhat permeable to molecules of the size of N₂ and is likely related to the size of the ethane bridges. The higher permeance of these molecules at higher temperatures and pressures can be explained by an increased flexibility of the organic bridges and correlates with a larger pore volume. A pervaporation process for the separation of H₂O from *n*-butanol showed a higher selectivity at smaller pore sizes.

In-situ study of the growth of the colloidal organosilica particles with SAXS pointed towards a Diffusion-Limited Cluster

Aggregation process under all acid-catalyzed conditions. The growth rate depended on the acid concentration, resulting in the formation of similar structures in the wet state. Drying at low acid concentration close to the isoelectric point resulted in a structure that was homogeneous on the 1–10 nm scale. This is related to collapse of the colloidal structure by Van der Waals and capillary forces. Even for a continuous network gel, the network strength was insufficient to resist collapse to a microporous system with very small pores. At high acid concentration, a Reaction-Limited Cluster Aggregation process was observed during solvent evaporation. Increased network strength due to ongoing condensation reactions and a positive charge on the colloidal particles resulted in a structure with larger pores. The pore structure was not related to the colloid size at the onset of drying.

The solvolytical stability in water, acids, or bases of each of the materials was an order of magnitude better than that of silica. We thus demonstrated that the size selectivity of organically bridged silica membranes can be varied by adjustment of the acid concentration prior to membrane fabrication. This offers excellent prospects for application in a broad range of industrial molecular separations.

Acknowledgments

This research was supported by the Netherlands Technology Foundation STW and the EOS technology programme of the Dutch Ministry of Economic Affairs. We thank the Netherlands Organisation for Scientific Research (NWO) for providing us with the possibility of performing SAXS measurements at DUBBLE, and Giuseppe Portale at DUBBLE for on-site assistance.

Appendix A

List of symbols used throughout the text

q	modulus of scattering vector
I	scattering intensity
d_{hyd}	mean hydrodynamic diameter determined with dynamic light scattering
β	exponent from power-law relation $I \sim q^{-\beta}$ fitted to a SAXS pattern
L_C	correlation length
$A_{\text{N}_2/\text{CO}_2}$	surface area determined with N ₂ /CO ₂
p/p^0	relative vapor pressure
d_p	pore diameter determined by gas adsorption
v_p	pore volume determined by gas adsorption
t_m	thickness of organosilica membrane top-layer
P	gas permeability
α	separation factor for pervaporation process
E_{app}	apparent activation energy of gas transport through a membrane

Appendix B. Supplementary data

Supplementary data associated with this article can be found, in the online version, at <http://dx.doi.org/10.1016/j.micromeso.2013.11.005>.

References

- [1] I. Agirre, M.B. Guemez, A. Motelica, H.M. van Veen, J.F. Vente, P.L. Arias, *J. Chem. Technol. Biotechnol.* 87 (2012) 943–954.
- [2] P.D. Chapman, T. Oliveira, A.G. Livingston, K. Li, *J. Membr. Sci.* 318 (2008) 5–37.
- [3] R.Y.M. Huang (Ed.), *Pervaporation Membrane Separation Processes*, Elsevier Science, Amsterdam, The Netherlands, 1991.

- [4] N.K. Kanellopoulos (Ed.), *Recent Advances in Gas Separation by Microporous Ceramic Membranes*, Elsevier Science, Amsterdam, The Netherlands, 2000.
- [5] P. Bernardo, E. Drioli, G. Golemme, *Ind. Eng. Chem. Res.* 48 (2009) 4638–4663.
- [6] H.L. Castricum, A. Sah, R. Kreiter, D.H.A. Blank, J.F. Vente, J.E. ten Elshof, *Chem. Commun.* (2008) 1103–1105.
- [7] H.L. Castricum, A. Sah, R. Kreiter, D.H.A. Blank, J.F. Vente, J.E. ten Elshof, *J. Mater. Chem.* 18 (2008) 2150–2158.
- [8] J. Sekulic, A. Magraso, J.E. ten Elshof, D.H.A. Blank, *Microporous Mesoporous Mater.* 72 (2004) 49–57.
- [9] R.J.R. Uhlhorn, M. Intveld, K. Keizer, A.J. Burggraaf, *J. Mater. Sci.* 27 (1992) 527–537.
- [10] H.L. Castricum, R. Kreiter, H.M. van Veen, D.H.A. Blank, J.F. Vente, J.E. ten Elshof, *J. Membr. Sci.* 324 (2008) 111–118.
- [11] H.M. van Veen, M.D.A. Rietkerk, D.P. Shanahan, M.M.A. van Tuel, R. Kreiter, H.L. Castricum, J.E. ten Elshof, *J. Membr. Sci.* 380 (2011) 124–131.
- [12] M. Kanezashi, K. Yada, T. Yoshioka, T. Tsuru, *J. Am. Chem. Soc.* 131 (2009) 414–415.
- [13] M. Kanezashi, K. Yada, T. Yoshioka, T. Tsuru, *J. Membr. Sci.* 348 (2010) 310–318.
- [14] H. Qi, J. Hang, N. Xu, *J. Membr. Sci.* 382 (2011) 231–237.
- [15] H. Qi, J. Hang, N. Xu, H.J.M. Bouwmeester, *ChemSusChem* 3 (2010) 1375–1378.
- [16] R. Kreiter, M.D.A. Rietkerk, H.L. Castricum, H.M. van Veen, J.E. ten Elshof, *J.F. Vente, ChemSusChem* 2 (2009) 158–160.
- [17] H.L. Castricum, G.G. Paradis, M.C. Mittelmeijer-Hazeleger, R. Kreiter, J.F. Vente, J.E. ten Elshof, *Adv. Funct. Mater.* 21 (2011) 2319–2329.
- [18] R.K. Iler, *The Chemistry of Silica*, Wiley & Sons Inc., New York, USA, 1979.
- [19] C.J. Brinker, G.W. Scherer, *Sol–gel Science. The Physics and Chemistry of Sol-gel Processing*, Academic Press Ltd., San Diego, USA, 1990.
- [20] C. Okkerse, J.H. de Boer, *J. Chim. Phys. Phys.-Chim. Biol.* 57 (1960) 534–542 (in French).
- [21] R.Yu. Sheinfain, *Kolloidn Zh* 23 (1961) 756–760.
- [22] R.Yu. Sheinfain, J.E. Neimark, *Kinet. Katal.* 8 (1967) 433–440.
- [23] R.Yu. Sheinfain, O.P. Stas', T.F. Makovskaya, *Kolloidn Zh* 34 (1972) 976–978.
- [24] D. Dollimore, G.R. Heal, *Faraday Soc. Trans.* 59 (1963) 2386–2393.
- [25] R.S.A. De Lange, J.H.A. Hekkink, K. Keizer, A.J. Burggraaf, *J. Non-Cryst Solids* 191 (1995) 1–16.
- [26] B.N. Nair, W.J. Elferink, K. Keizer, H. Verweij, *J. Colloid Interface Sci.* 178 (1996) 565–570.
- [27] W.J. Elferink, B.N. Nair, R. de Vos, K. Keizer, H. Verweij, *J. Colloid Interface Sci.* 180 (1996) 127–134.
- [28] B.N. Nair, J.W. Elferink, K. Keizer, H. Verweij, *Sci. Technol.* 8 (1997) 471–475.
- [29] B.N. Nair, K. Keizer, T. Okubo, S.I. Nakao, *Adv. Mater.* 10 (1998) 249–252.
- [30] B.N. Nair, K. Keizer, H. Suematsu, Y. Suma, N. Kaneko, S. Ono, T. Okubo, S.-I. Nakao, *Langmuir* 16 (2000) 4558–4562.
- [31] D.A. Loy, K.J. Shea, *Chem. Rev.* 95 (1995) 1431–1442.
- [32] K.J. Shea, D.A. Loy, *Chem. Mater.* 13 (2001) 3306–3319.
- [33] R.J.P. Corriu, M. Granier, G.F. Lanneau, *J. Organomet. Chem.* 562 (1998) 79–88.
- [34] G. Dubois, W. Volksen, T. Magbitang, R.D. Miller, D.M. Gage, R.H. Dauskardt, *Adv. Mater.* 19 (2007) 3989–3995.
- [35] W. Volksen, R.D. Miller, G. Dubois, *Chem. Rev.* 110 (2010) 56–110.
- [36] B. Hatton, K. Landskron, W. Whitnall, D. Perovic, G.A. Ozin, *Acc. Chem. Res.* 38 (2005) 305–312.
- [37] N. Mizoshita, T. Tani, S. Inagaki, *Chem. Soc. Rev.* 40 (2011) 789–800.
- [38] G. Smeulders, V. Meynen, A. Silvestre-Albero, K. Houthoofd, M. Mertens, J. Silvestre-Albero, J.A. Martens, P. Cool, *Mater. Chem. Phys.* 132 (2012) 1077–1088.
- [39] B.C. Bonekamp, *Fundamentals of Inorganic Membrane Science and Technology*, in: A.J. Burggraaf, L. Cot (Eds.), vol. 4, Elsevier, Amsterdam, The Netherlands, 1996 (Chapter 6).
- [40] H.M. van Veen, Y.C. van Delft, C.W.R. Engelen, P.P.A.C. Pex, *Sep. Purif. Technol.* 22–23 (2001) 361–366.
- [41] W. Bras, I.P. Dolbnya, D. Detollenaere, *J. Appl. Crystallogr.* 36 (2003) 791–794.
- [42] W. Bras, G.E. Derbyshire, A. Devine, S.M. Clark, J. Cooke, B.E. Komanschek, A.J. Ryan, *J. Appl. Crystallogr.* 28 (1995) 26–32.
- [43] T.M. Stawski, S.A. Veldhuis, H.L. Castricum, E.G. Keim, G. Eeckhaut, W. Bras, D.H.A. Blank, J.E. ten Elshof, *Langmuir* 27 (1089) (2011) 11081–11089.
- [44] G. Porod, *Small Angle X-ray Scattering*, vol. 15, Academic Press, New York, USA, 1982, p. 515.
- [45] M.G. Kaganer, *Zh. Fiz. Khim.* 33 (1959) 2202.
- [46] S.J. Gregg, K.S.W. Sing, *Adsorption, Surface Area and Porosity*, Academic Press, London, UK, 1982.
- [47] J. Teixeira, *J. Appl. Crystallogr.* 21 (1988) 781–785.
- [48] S.H. Chen, J. Teixeira, *Phys. Rev. Lett.* 57 (1986) 2583–2586.
- [49] C.J. Brinker, T.L. Ward, R. Seghal, N.K. Raman, S.L. Hietala, D.M. Smith, D.-W. Hua, T.J. Headly, *J. Membr. Sci.* 77 (1993) 165–179.
- [50] N. Meane, B.N. Nair, P. D'Hooghe, S.-I. Nakao, K. Keizer, *J. Sol–Gel Sci. Technol.* 12 (1998) 117–134.
- [51] M.Y. Lin, H.M. Lindsay, D.A. Weitz, R.C. Ball, R. Klein, P. Meakin, *Proc. R. Soc. London, Ser. A* 423 (1989) 71–87.
- [52] P. Meakin, *J. Sol–Gel Sci. Technol.* 15 (1999) 97–117.
- [53] V. Boffa, J.E. ten Elshof, A.V. Petukhov, D.H.A. Blank, *ChemSusChem* 1 (2008) 437–443.
- [54] V. Boffa, H.L. Castricum, R. Garcia, R. Schmuhl, A.V. Petukhov, D.H.A. Blank, J.E. ten Elshof, *Chem. Mater.* 21 (2009) 1822–1828.
- [55] D.W. Schaefer, *Science* 234 (1989) 1023–1027.
- [56] R.-J. Roe, *Methods of X-ray and Neutron Scattering in Polymer Science*, Oxford University Press, New York, USA, 2000.
- [57] J.C. Vedrine, A. Auroux, V. Bolis, P. Dejaive, C. Naccache, P. Wierzbowski, E.G. Derouane, J.B. Nagy, J.-P. Gilson, J.H.C. van Hooff, J.P. van den Berg, J. Wolthuizen, *J. Catal.* 59 (1979) 248–262.
- [58] J. Rudolph, H. Zimmermann, *Z. Phys. Chem.* 43 (1964) 311–326 (in German).
- [59] R.M. de Vos, H. Verweij, *Science* 279 (1998) 1710–1711.
- [60] J. Campaniello, C.W.R. Engelen, W.G. Haije, P.P.A.C. Pex, J.F. Vente, *Chem. Commun.* (2004) 834–835.
- [61] G. Beamsom, D. Briggs, *High Resolution XPS of Organic Polymers: The Scienta ESCA300 Database*, John Wiley & Sons, Chichester, UK, 1992, p. 268.
- [62] V. Boffa, J.E. ten Elshof, D.H.A. Blank, *J. Membr. Sci.* 319 (2008) 256–263.
- [63] C.M. Jephcott, J.H. Johnston, *AMA Arch. Ind. Hyg. Occup. Med.* 1 (1950) 323–340.
- [64] E.V. Ballou, M.I. Leban, T. Wydeven, *J. Appl. Chem. Biotechnol.* 23 (1973) 119–130.
- [65] J. Sekulic, J.E. ten Elshof, D.H.A. Blank, *J. Membr. Sci.* 254 (2005) 267–274.
- [66] R.M. de Vos, H. Verweij, *J. Membr. Sci.* 143 (1998) 37–51.
- [67] K.-S. Chiang, T. Yoshioka, M. Kanezashi, T. Tsuru, K.-L. Tung, *Chem. Commun.* (2010) 9140.
- [68] K.-S. Chang, T. Yoshioka, M. Kanezashi, T. Tsuru, K.-L. Tung, *J. Membr. Sci.* 381 (2011) 90–101.
- [69] C.J. Brinker, G.C. Frye, A.J. Hurd, C.S. Ashley, *Thin Solid Films* 201 (1991) 97–108.
- [70] B. Derjaguin, L. Landau, *Acta Physico Chemica URSS* 14 (1941) 633–662.
- [71] E.J.W. Verwey, J.Th.G. Overbeek, *Theory of the Stability of Lyophobic Colloids*, Elsevier, Amsterdam, The Netherlands, 1948.
- [72] F. Dumont, *Adv. Chem. Ser.* 234 (1994) 143–146.

ECN

Westerduinweg 3
1755 LE Petten
The Netherlands

P.O. Box 1
1755 LG Petten
The Netherlands

T +31 88 515 4949
F +31 88 515 8338
info@ecn.nl
www.ecn.nl